Geothermal Energy

RESEARCH Open Access

Geophysical characteristics of a fault system in the northern Central Range of Taiwan and its applications for geothermal energy exploration

Bing-Cheng Chen[1,2], Tito Perdana[3] and Li-Wei Kuo[1,4,5*]

*Correspondence:
liweikuo@ncu.edu.tw;
liweikuo@gmail.com

[1] Department of Earth Sciences, National Central University, No. 300, JhongDa Rd., Jhongli District, Taoyuan City 32001, Taiwan
[2] CPC Corporation Taiwan, Taipei, Taiwan
[3] GeothermEx Inc, a Schlumberger Company, Richmond, CA, USA
[4] Earthquake-Disaster & Risk Evaluation and Management Center, National Central University, No. 300, JhongDa Rd., Jhongli District, Taoyuan City 32001, Taiwan
[5] Carbon Storage and Geothermal Research Center, National Central University, No. 300, JhongDa Rd., Jhongli District, Taoyuan City 32001, Taiwan

Abstract

The northern Central Range of Taiwan is a high-potential geothermal region. Since the formations are mainly tight metasandstone and slate, permeable structures associated with faults are commonly considered as conduits of geothermal fluids. This study determines the characteristics and orientations of the permeable fault zones by analyzing the geophysical logs and microresistivity formation image log (FMI) of the JT-4 well in Jentse, an important geothermal area in the northern Central Range. Between 720 and 1480 m measured depth (MD), the effective porosity of the intact host rock is mostly below 3% calculated by the geophysical log. Zones with porosity greater than 5% are only clustered within a few thin intervals. The FMI interpretations show these porous zones are in the interior of the fractured and faulted intervals. These porous fault zones comprise fault damage zones with a high density of open fracture planes and fault cores with porous fault breccias. There is a highly brecciated fault core in 1334–1339 m MD, which would be the most permeable interval of the well. Additionally, some healed fault zones with sealed fractures are observed. The picked drilling-induced tensile fractures signify that the direction of the present-day maximum horizontal principal stress is N40–50°E, and most of the open fractures also strike parallel to the NE–SW direction. The study results show that the open fractures are concentrated in the four fault zones belonging to one major normal fault system. After integrating the orientations and locations of the fault zones, we propose that the permeable normal fault system is about 200 m wide, trends N50–70°E, and dips 70–80° to the NW. The development of the open fractures and the permeable fault system in the northern Central Range may be controlled by the current rifting of the Okinawa Trough offshore northeastern Taiwan. The study exhibits the characteristics of fractured fluid conduits of the regional geothermal system, which will benefit future geothermal exploration in northeastern Taiwan.

Keywords: Central Range Taiwan, Fractured zones, Borehole image logs, Petrophysical logs, Temperature logs, Fault system

Introduction

Geothermal fields in the world exist in various geological environments (Moeck 2014). Although the production of geothermal fluids in high porosity is more economical, high permeability reservoirs and geothermal resources can also exist in low porosity,

low permeability formations. In tight formations, geothermal fluids are mainly produced from permeable fractures (Rowland and Sibson 2004; Tong et al. 2008; Yamada et al. 2000). Permeable structures that can produce geothermal fluids are often associated with faults (Jolie et al. 2015; Taguchi and Nakamura 1991). Moreover, although subsurface permeable fractures often develop along faults, not all faults contain permeable internal structures (Caine et al. 1996; Rowland and Sibson 2004; Faulkner et al. 2010; Houwers et al. 2015). The existing permeable fractures within fault zones can transform to impermeable fractures due to later mineral filling (Ameen 2014; Liotta et al. 2021) or be closed due to stress changes (Barton and Zoback 2002). Therefore, to analyze geothermal fields based on fracture conduits, the internal structures of subsurface fault zones need to be understood.

At shallow depth, a brittle fault zone commonly contains three major internal components: fault core, damage zone, and host rock (Caine et al. 1996). The host rock is basically undamaged, while the damage zone is characterized by fractures and veins. The fault core is typically characterized by geochemically altered and comminuted rocks. Along with the faulting processes, damage zones and fault cores usually develop and evolve within fault zones (e.g., Kuo et al. 2009, 2014, 2017). Therefore, fault cores and fault zones commonly exhibit different physical and chemical properties in different geological setting (Bense et al. 2013; Caine et al. 1996; Faulkner et al. 2010). Fault cores and fault damage zones exhibit distinct responses in geophysical logs and microresistivity formation image (FMI) logs (Chen et al. 2021; Hamahashi et al. 2015; Jeppson et al. 2010; Lyu et al. 2017). Geophysical logs are measurements of physical properties of rocks, such as lithology and porosity, made in boreholes by wireline logging tools. Geophysical logs and FMI logs are considered as two of the most common tools for observing subsurface fault zones and their internal properties (Li et al. 2022). This study utilizes geophysical logs and FMI logs to determine the relationships between geothermal potentials and fault zones.

Taiwan experiences high heat flow and is suitable for geothermal energy production (Liu et al. 2015; Song and Lu 2019). The northern Central Range in northeastern Taiwan, comprising several known geothermal prospects, has been considered promising for geothermal energy production (Song and Lu 2019; Tong et al. 2008). In the northern Central Range, hot springs are mainly located in the tight slate belt; thus, open fractures have long been considered efficient conduits for geothermal water production (Hsiao and Chiang 1979; Tseng 1978). Geophysical surveys have suggested that geothermal water circulations in this region is related to permeable fault zones (Chang et al. 2014; Chiang et al. 2015; Tong et al. 2008). Thus, discovering permeable faults and understanding their permeability characteristics are crucial for geothermal exploration and development in this region.

To determine the locations and characteristics of underground productive faults of geothermal fluids, CPC Corporation Taiwan drilled two geothermal exploration wells, JT-3 and JT-4, in the Jentse geothermal area in the North Central Range from 2018 to 2019. The drilling results of the JT-3 well show that a fault system with permeable fractures was penetrated by the well (Chen et al. 2021). This study utilizes the geophysical logs and FMI image logs of the JT-4 well to determine the location and permeability characteristics of subsurface faults and fractures. Additionally, the data of this study

provide more reliable information on the petrophysical characteristics of the slate belt of Taiwan. The collected data and results will be beneficial for geothermal exploration and development in northeastern Taiwan.

Geological background

Tectonic setting

The island of Taiwan was formed due to the collision between the Philippine Sea Plate and the Eurasian Plate in the late Miocene (Angelier et al. 2009; Shen et al. 2020; Shyu et al. 2005; Teng 1996; Teng and Lin 2004). Moreover, the tectonic collision formed metamorphic rocks, compressional structures, and a high mountain landscape in the northern Central Range. In northeastern Taiwan, the Philippine Sea Plate is submerging beneath the Eurasian Plate, leading to the development of the Ryukyu arc–trench system. In this system, the Okinawa Trough is a back-arc basin that extends eastward into northeastern Taiwan (Fig. 1). Since the late Pleistocene, the gradual eastward rifting of the Okinawa Trough has caused the development of the Ilan plain and the regional extension in northeastern Taiwan (Shen et al. 2020; Lai et al. 2009). Additionally, northern Taiwan has experienced post-collisional extension since 2 Ma and has transformed into an extensional tectonic environment (Hsu et al. 2009; Huang et al. 2012; Lai et al. 2009; Teng 2004, 1996). Furthermore, the past boundary thrust fault between the northern Central Range and the Huseshan Range, the Lishan Fault, is believed to be a normal

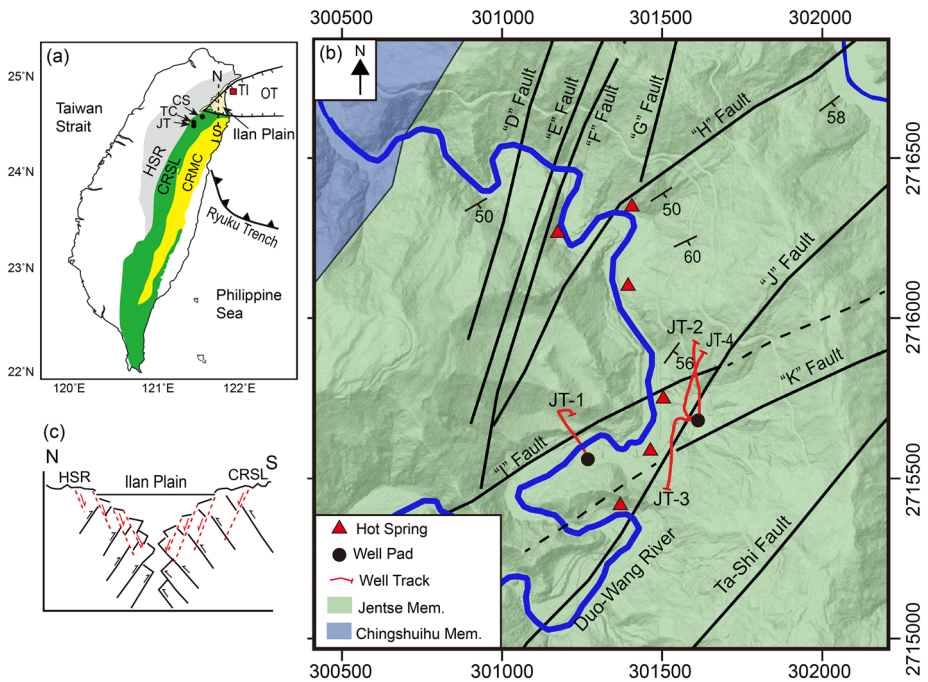

Fig. 1 Location of the Jentse geothermal area. **a** Geological setting of the study region (*CRMC* the metamorphic complex of the Central Range, *CRSL* the slate belt of the Central Range, *CS* Chinshui, *JT* Jentse, *HSR* the Hsueshan Range, *OI* the Okinawa Through, *TC* Tuchang, *TI* the Turtle Island). The boundary between CRMC and HSR is the Lishan Fault. **b** Simplified geological map of the Jentse area (modified from Chang et al. 1986). **c** The N–S simplified profile shown in **a**. Black solid lines are reverse faults and red dashed lines are normal faults (modified from Shyu et al. 2005)

fault (Lee et al. 1997; Su et al. 2018). Due to the recent regional extension, other normal faults may have developed under and around the Ilan Plain (Shen et al. 2020; Shyu et al. 2005). Both compressional and extensional structures may be present in the northern Central Range due to the early collision and recent extension.

The abundance of geothermal manifestations in the northern Central Range indicates the high geothermal potential of this region (Liu et al. 2015; Song et al. 2019). To date, three major geothermal prospects have been confirmed in the northern Central Range: Chinshui, Tuchang, and Jentse (from north to south; Fig. 1). Recent geophysical and geochemical studies indicated the possible presence of rifting-related heat sources in this area (Lu et al. 2017; Tong et al. 2008). Additionally, the undissipated heat of the rapidly uplifted metamorphic rock has been suggested as a possible geothermal heat source of this region (Lin 2000; Chen 1985; Yu et al. 1993). Borehole temperature measurements and geochemical thermometer show that the formation temperature is up to 200–230 °C at depths of 2000–3000 m in this region (Huang et al. 2018; Liu et al. 2015).

The surface of geothermal areas in the northern Central Range is dissected by a series of NE–SW and N–E trending joints, faults, and folds (Hsiao and Chiang 1979; Lin, 1995; Tseng 1978). These studies indicated that the geothermal conduits in this region are either faults or fractures. However, geophysical studies and drilling results have suggested that only some faults are effective for the economic production of geothermal fluids (Chang et al. 2014; Chiang et al. 2015; Tong et al. 2008). Several geophysical and geochemical studies have been conducted in the northern Central Range to find subsurface geothermal productive faults (Chang et al. 2014, 2020; Chiang et al. 2015; Ho et al. 2014; Lu et al. 2018, 2020; Tong et al. 2008). However, verifying which faults are better suited for geothermal production is difficult via surface surveys. To verify the locations and properties of the subsurface faults, more geological data are required directly from the subsurface. This study attempts to acquire the properties of the subsurface faults in the Jentse geothermal area using the log data of the JT-4 well to reveal the characteristics of geothermal conduit faults.

A series of NE–SW and N–E trending faults were observed on the surface of the Jentse area (Fig. 1). Some of these faults are associated with the geothermal manifestation locations (Hsiao and Chiang 1979; Lin and Lin 1995; Tseng 1978). Although this needs to be confirmed using subsurface data, these faults are believed to be the geothermal conduits connected to the subsurface permeable faults. Due to the poor outcrop continuity, the orientations and extents of these faults still need to be determined. In the absence of drill holes penetrating the subsurface fault zones, verifying which of the observed faults are effective geothermal migration paths is difficult.

Lithology

The western flank of the Central Range comprises the Miocene slate belt, the Lushan Formation, which extends in a nearly N–S orientation for several hundred kilometers with a width of at least 14 km in the E–W direction (Fig. 1). The Lushan formation is mainly composed of slate and a small proportion of metasandstone (Lin, 1995). The Lushan Formation is divided into the Kulu Member, Chinshuihu Member, and Jentse Member from bottom to top according to the different ratios of the slate beds (Hsiao and Chiang 1979). The Kulu Member and Chinshuihu Member primarily contain slate,

whereas the Jentse Member contains higher proportions of metasandstone. In the Jentse geothermal area, located in the Jentse Member, the formations strike at approximately N30°–80°E and dip 30°–90°SE. Some strata are nearly vertical or steeply overturned toward the NW with similar strikes (Hsiao and Chiang 1979; Chen et al. 2021).

Compared to other parts of the Lushan Formation, the Jentse Member exhibit a relatively low degree of metamorphism (Chen et al. 2019). Most of their bed boundaries and sedimentary structures did not deform during the metamorphic process, and cleavages are only weakly developed. The low-grade metamorphic rocks of the Lushan Formation were originally distal marine shale and sandstone. Therefore, the occurrence of rocks resembles that of interbedded tight shale and sandstone strata. Thus, the geophysical log data and FMI borehole images at Jentse should be similar to those of tight sandstone and shale.

History of geothermal exploration at Jentse

The first geothermal explorations at Jentse and the nearby Tuchang area were conducted in the 1970s and 1980s (Chang et al. 1986; Hsiao and Chiang 1979; Su 1978; Tseng 1978). Then, the CPC Corporation, Taiwan drilled two deep geothermal exploration wells at Jentse (the JT-1 and JT-2 wells) to depths of up to 2277 m in 1983 and 1984. In the well JT-2, the highest static formation temperature of 218 °C was recorded at about 2000 m measured depth (MD) (CPC 1984). No further drilling was undertaken as it was difficult to find other flat ground areas to drill during this time. The JT-1 and JT-2 wells have been used for producing hot water for tourism until now.

Drilling data of wells JT-1 and JT-2 have indicated that potentially permeable fracture zones are passing through the boreholes below 800 m MD (Lee and Lee 1983; CPC 1984). These penetrated fracture zones have been hypothesized to be parts of underground fault zones. However, at that time, the properties of the underground fractures had been uncertain due to the lack of reliable modern log data. In 2018 and 2019, CPC drilled JT-3 and JT-4 wells with 1475 m MD and 1500 m MD, respectively, using the well pad of the JT-2 well. The JT-3 and JT-4 wells, which deviated to the south and north, were designed to target the fracture zones that were penetrated by the previous JT-1 and JT-2 wells. The production test of the JT-3 well showed that the production rate was 48 tons/h at the wellhead pressure of 3.3 bar, a wellhead temperature of 138 °C, and a static bottom-hole temperature of about 180 °C (Chen et al. 2021). Data from the JT-3 well showed that it penetrated a permeable fault system south of the well pad with an orientation of N50°–70°E and dip of 70°–80° NW (Chen et al. 2021).

This study utilizes the data from the JT-4 well to determine the characteristics of the underground fractures north of the well pad. This study believes that if the location of the fault system penetrated by the JT-3 well is reliable, the JT-4 well would also penetrate the same fault system. By obtaining more data and observations, this study would provide a better understanding of the Jentse geothermal system.

Data and study methods

Background information of well JT-4

The JT-4 well is a directional well that deviates toward the north. From 0 to 700 m MD, the angle of borehole inclination gradually increases from 2 to 20° toward the north.

Then, to trace the possible permeable fault zones, from 720 to 1500 m MD (8.5-inch-diameter interval), the angle of borehole inclination gradually decreases from 20 to 3° toward the north. Fracture zones in the 720–1500 m MD well section elucidated by the geophysical logs and FMI borehole images were selected for slotted liner placement. Moreover, a 13-day flow test was conducted in the JT-4 well using the James lip pressure method. The stable production rate of the well was 56 tons/h at 3.3 bar-g wellhead pressure and 141 °C wellhead temperature. The static formation temperature, measured 92 days after the wellbore shut-in, was approximately 174–204 °C in the 700–1480 m MD interval (Fig. 2).

This study utilized various log data of the JT-4 well to investigate the fault zone and fracture characteristics. The studied log data were acquired from the 720 to 1480 m MD well interval within the 8.5-inch-diameter interval. The employed logs include the temperature logs, geophysical logs, and FMI borehole image log. The geophysical logs used included caliper, gamma ray (*GR*), deep resistivity (*RT*), neutron porosity (*NPHI*), bulk density (*RHOB*), and sonic slowness (*DT*) logs (Fig. 3). Three temperature logs were surveyed in the borehole filled with drilling mud at 34, 51, and 61 h after the completion of drilling (Fig. 2). The other temperature log (92D log) was surveyed after the well shut-in for 92 days and was surveyed in the borehole filled with clean water.

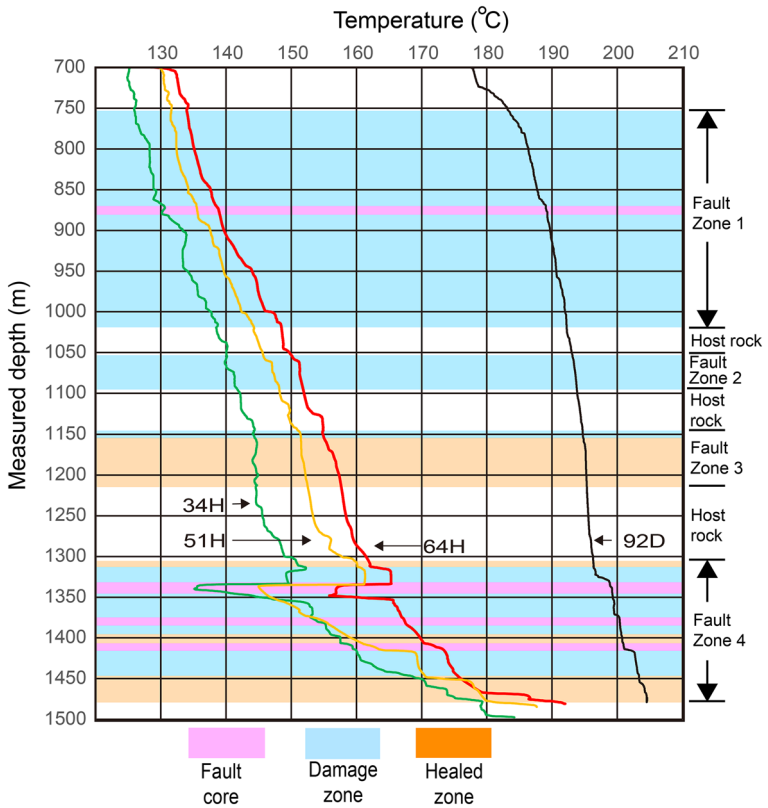

Fig. 2 Temperature logs of the studied well section. The 34H, 51H, and 61H logs were surveyed in drilling mud 34, 51, and 61 h after the end of drilling. The 92D log was surveyed after the mud in the well was replaced by clean water and shut-in for 92 days. The drastic temperature changes in the 1334–1346 m MD and 1405–1410 m MD intervals could be related to the fault cores of Fault Zone 4

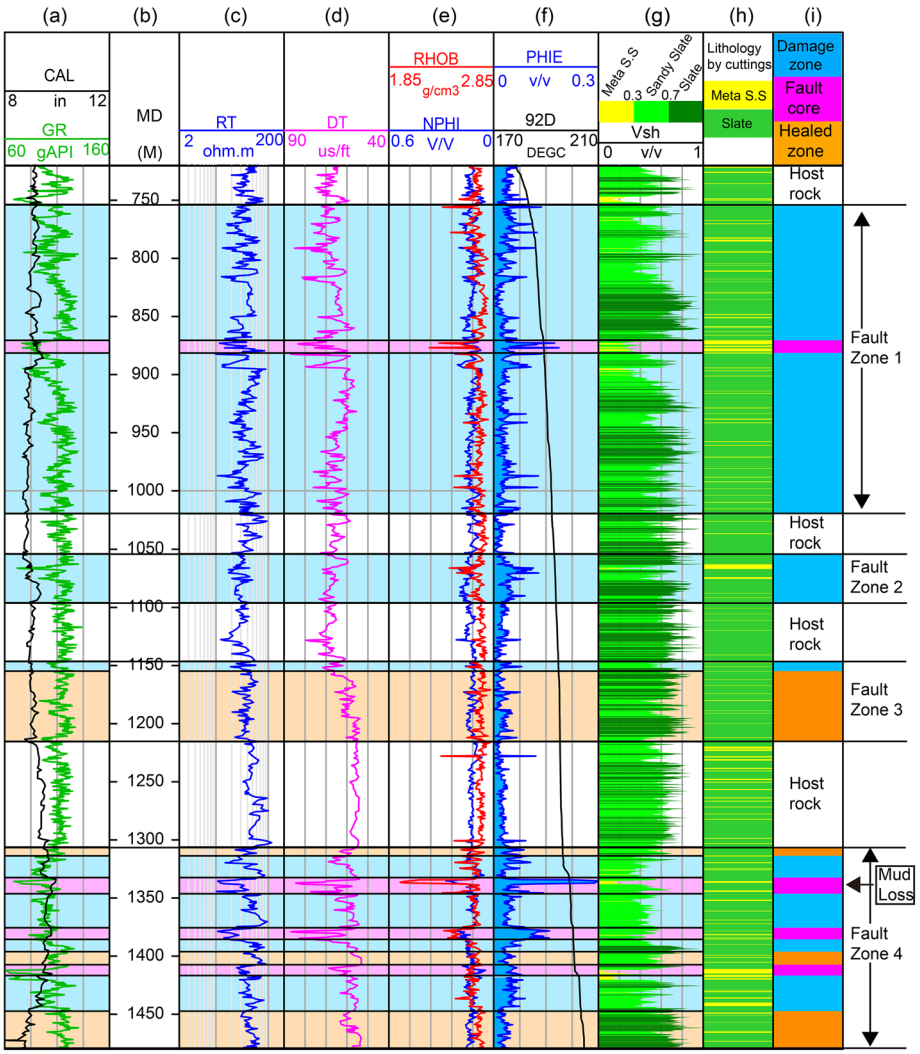

Fig. 3 Geophysical logs used in this study and the interpreted results (*CAL* caliper, *GR* gamma ray, *MD* measured depth, *RT* deep resistivity, *DT* sonic slowness, *RHOB* bulk density after reconstruction, *NPHI* neutron porosity after reconstruction, *PHIE* effective porosity, *92D* temperature log after shut-in for 92 days; and *Vsh*: shale volume). The column (h) is the lithology interpreted by the cuttings description, and the column (i) is the interpreted zones

Since subsurface fracture plane apertures are commonly at the millimeter scale, the resolution of the current modern geophysical logs often could not detect a single fracture plane (Crain 2023). However, the logs may still have responses to fracture zones if overall changes in the petrophysical properties of the fractured zones are significant enough (Hamahashi et al. 2015; Jarzyna et al. 2021; Jeppson et al. 2010; Lyu et al. 2017; Townend et al. 2013). Furthermore, till date, FMI image logs have been an efficient and reliable tool for continuously observing fractures in boreholes. Therefore, this study utilized the FMI image logs to obtain reliable images of borehole surfaces to delineate the bedding and structural features of the studied borehole interval.

Workflow of geophysical log data analysis

Quality check of the geophysical logs

Before interpretation, the geophysical logs were examined following the depth matching and abnormal value checking procedures. Abnormal log values are usually caused by electrical or mechanical engineering issues or borehole irregularities. After checking the logs, there were no values that were considered unusual or outside of what was expected. Therefore, there was no process conducted to remove any values before interpretation.

Due to the low degree of metamorphism, the occurrence of slate and metasandstone at Jentse remains similar to that of tight shale and sandstone (Chen et al. 2019). Therefore, the log interpretation workflow for sand/shale was performed during the geophysical log interpretations. The procedures included shale volume (*Vsh*) calculation, lithology interpretation, and effective porosity (*PHIE*) calculations. The water saturation value was set as one as no hydrocarbons are present in this area.

Shale volume calculations and lithology interpretations

This study utilizes the *GR* logs to calculate *Vsh* and construct the lithology column. The *Vsh* value represents the proportion of shale in a unit rock volume, and it can be calculated using Eq. (1) (Crain 2023):

$$Vsh = \frac{GR_{\log} - GR_{\min}}{GR_{\max} - GR_{\min}}, \tag{1}$$

where $GR_{\log}$ is *GR* log reading (API), $GR_{\min}$ is *GR* value assigned for pure metasandstone (API), and $GR_{\max}$ is *GR* value assigned for pure slate (API). In addition to the *Vsh* calculation by the *GR* log, cross-plotting of the *NPHI* and *RHOB* logs accompanied by *GR* log values is also a common way for observing the log responses to lithology and porosity (Crain 2023). In this study, a crossplot was generated to observe the relations among log values, lithology, and porosity (Fig. 4).

Workflow of the FMI image log analysis

Effective porosity (PHIE) calculations

However, because shale volumes also affect the *RHOB* and *NPHI* log values, directly using these two logs as porosity indicators would be biased by shale volumes. The *PHIE* log calculated from the *RHOB*, *NPHI* and *Vsh* logs is commonly used to exclude the responses of shale volumes in the *RHOB* and *NPHI* logs (Crain 2023). Thus, this study believes that the *PHIE* log is a good indicator of fracture space development. The *PHIE* log was generated using Eqs. (2, 3, 4, 5) according to Crain (2023):

$$PHIE = \frac{PHIE_n + PHIE_d}{2}, \tag{2}$$

where $PHIE_n$ is effective porosity derived from *NPHI* (*v*/*v*), and $PHIE_d$ is effective porosity derived from *RHOB* (*v*/*v*). The values of $PHIE_n$ and $PHIE_d$ were derived by Eqs. (3) and (4), respectively:

$$PHIE_n = NPHI_{\log} - Vsh \times NPHI_{\mathrm{sh}}, \tag{3}$$

where $NPHI_{\log}$ is *NPHI* log reading (*v*/*v*), and $NPHI_{\mathrm{sh}}$ is *NPHI* log value of pure slate (*v*/*v*),

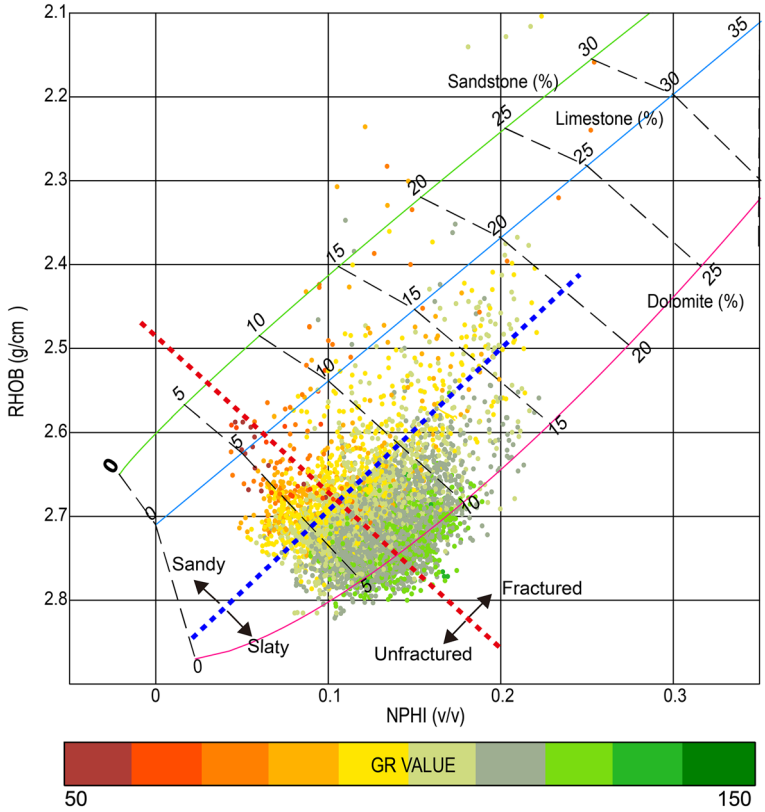

Fig. 4 Crossplot of the *NPHI* and *RHOB* log values with the colors representing the *GR* log values. Based on the *GR* values, the upper left side of the thick blue dashed line comprises metasandstone and sandy slate and the lower right side of the blue dashed line comprises slate. The unfractured rocks have low *NPHI* and high *RHOB* and are present to the left side of the red dashed line. The fractured porous rocks mainly have high *NPHI* and low *RHOB* and are present to the right side of the red dashed line

$$PHIE_d = PHID - Vsh \times PHID_{\mathrm{sh}}, \tag{4}$$

where *PHID* is total density porosity derived from the *RHOB* log reading (v/v) and $PHID_{sh}$ is total density of pure slate derived from the *RHOB* value (v/v). *PHID* was calculated from *RHOB* as follows:

$$PHID = \frac{RHOB_{\mathrm{ma}} - RHOB_{\mathrm{log}}}{RHOB_{\mathrm{log}} - RHOB_{\mathrm{fl}}}, \tag{5}$$

where $RHOB_{\mathrm{ma}}$ is *RHOB* value of pure metasandstone (g/cm^3), $RHOB_{\mathrm{log}}$ is *RHOB* log reading (g/cm^3), and $RHOB_{\mathrm{fl}}$ is *RHOB* value of formation fluid (g/cm^3).

Raw data processing and image data quality

The raw FMI borehole image data were processed before data interpretation. The procedures included inclinometry checking, depth matching, image equalization, and normalization (Schlumberger 2015). The quality of the processed images was good. The images well displayed the clear planar features of the bed boundaries and natural fracture planes, with the exception of a few short intervals with poor data quality. Overall,

the quality of the processed FMI image of the studied well interval was reliable for interpreting the fractures and bedding structures.

Procedures of the FMI image interpretations

Since bed boundaries are key reference features in the FMI interpretation, we selected bed boundaries every 1–2 m and analyzed the changes in the bedding orientation. Systematic smooth rotations of the bed orientations over a long well interval were used as indicators of the large-scale trends of the structural features. Abrupt drastic changes in bed orientations over a short interval often indicate severe shear/faulting.

In addition to beddings, fracture planes are common features in FMI images. Since almost no clay minerals precipitated within the fracture planes, the dark-colored fracture planes are regarded as natural open fracture planes herein because of the invasion of low-resistivity water-based drilling mud. In contrast, sealed fracture planes often appear as bright-colored sinusoids because of the filled high-resistivity mineral cements. In addition to the natural fracture planes, other fracture features, such as fault breccia, were identified.

The most common two drilling-related fracture features on borehole surfaces are drilling-induced tensile fractures and borehole breakouts. Generally, drilling-induced tensile fractures are parallel to the direction of the maximum horizontal principal stress. In contrast, the strike direction of borehole breakouts is usually parallel to the orientation of the minimum horizontal principal stress. These features are good indicators for verifying the local stress field directions (Barton and Zoback 2002; Peška and Zoback 1995; Zoback 2007).

Fracture density, fracture aperture, and fracture porosity

Using the picked open fracture planes, 1) fracture density (number of fractures per meter), 2) fracture aperture (apertures of fracture planes), and 3) fracture porosity (volume within the apertures of fracture planes per unit borehole volume) are calculated. These parameters are often used as indicators of fluid productivity of fractured reservoirs (Ameen 2014; Crain 2023; Schlumberger 2015).

In this study, the fracture density was calculated by the average number of fractures in 1-m sliding window length. As the angle between the fracture and borehole orientations increases, the number of fractures in the formations is increasingly underestimated (Priest 1993; Schlumberger 2015). Therefore, the fracture densities were corrected for the relations between the fracture and borehole orientations using the Terzaghi correction method (Terzaghi 1965). The maximum angle between the poles to the fractures and borehole was set as 85°. The fracture apertures were estimated using the resistivity values contained in the FMI borehole image log and the mud resistivity (Luthi and Souhaite 1990; Schlumberger 2015).

Image interpretations of breccia zones

In addition to the different types of fracture planes, fault breccia is another type of fracture structure in the studied well section. The porous fault breccia zones in the studied well section primarily comprise rock fragments (bright color) and void spaces (dark color). The porous breccia zones all exhibit extremely high *PHIE* log values, confirming

their porous nature. If the rock fragments are filled with quartz or calcite, the image of the fractures would be in bright color. In this case, the intervals were categorized into the internal structures of healed fault zones.

Data integration and zonation

After fracturing or faulting by the geologic processes, some intervals of host rocks may remain intact while others may be severely fractured. These fractured rocks can be fault gouges, angular rock fragments, or rocks dissected by discrete fracture planes. On the basis of interpreting and integrating of geophysical logs and FMI borehole image logs, the studied well section was divided into distinct zones based on the fracture characteristics. The fracture intensities of the different zones were recognized as the possible productive intervals of geothermal fluids for further exploitation.

Results

Results of geophysical log interpretations

The crossplot of *GR*, *RHOB*, and *NPHI* shows that the unfractured tight metasandstone has low *GR*, high *RHOB*, and low *NPHI* log values and the unfractured tight slate has high *GR*, high *RHOB*, and high *NPHI* log values (Fig. 4). Both the fractured metasandstone and slate have lower *RHOB* and higher *NPHI* log values than the unfractured ones. Note that the *GR* log values did not change due to fracturing, signifying that the fractured rocks do not contain many altered clay minerals.

The *GR* log values of the studied well section were mainly between 80 and 110 API. The *Vsh* log was compiled using Eq. (1) and the *GR* log values. Based on the calculated Vsh values, three rock types were classified: 1) metasandstone ($0 \leq Vsh \leq 0.3$), 2) sandy slate ($0.3 < Vsh \leq 0.7$), and 3) slate ($0.7 < Vsh \leq 1$) (Fig. 3). The interpreted lithology shows that the studied well section is mainly slate with a relatively small amount of metasandstone. Comparison of the rock types defined by *Vsh* with the lithology interpreted by drill cuttings showed that the *Vsh* log generated using the *GR* log is a reliable indicator of lithology.

After generating the *Vsh* and lithology logs, the *NPHI*, *RHOB*, and *Vsh* logs were used to calculate the *PHIE* values. According to the core measurements, the porosity of the slate at Jentse is less than 0.01 (Chen et al. 2021). The tight slate in the JT-4 well also shows high *RHOB* log values and low *NPHI* log values indicating the low porosity. However, the void spaces generated by rock fracturing can yield low *RHOB* values and high *NPHI* values of the strata.

The results of *PHIE* values were below 3% in some intervals, such as 1025–1050 and 1225–1300 m MD, regardless of the rock types (Fig. 3). Such low values are typical of intact host rock in this region, including both metasandstone and slate. In some short intervals, the *PHIE* values were higher than 5% (e.g., 754–800 and 1075–1100 m MD) and were sometimes even higher than 10% in some short intervals (e.g., 872–874 and 1334–1339 m MD) (Fig. 3). The high *PHIE* values primarily signify porous fractured rocks. The developments of fractured rocks observed on the *PHIE* log were confirmed by the interpretation of the FMI images in this study.

Results of FMI images interpretations

Orientations of the bedding planes

In the studied well interval, the boundaries of the formation beds were clearly visible and were picked in the FMI image. In some short intervals, the beds abruptly rotated (e.g., 860–870, 1205, and 1334–1346 m MD). Such abrupt changes in bedding angles are regarded as local small-scale faulting. In addition to these abrupt changes in the orientations of the bed boundaries, the formation attitudes also shift in a smooth and general trend (Figs. 5 and 6). The trend is as follows:

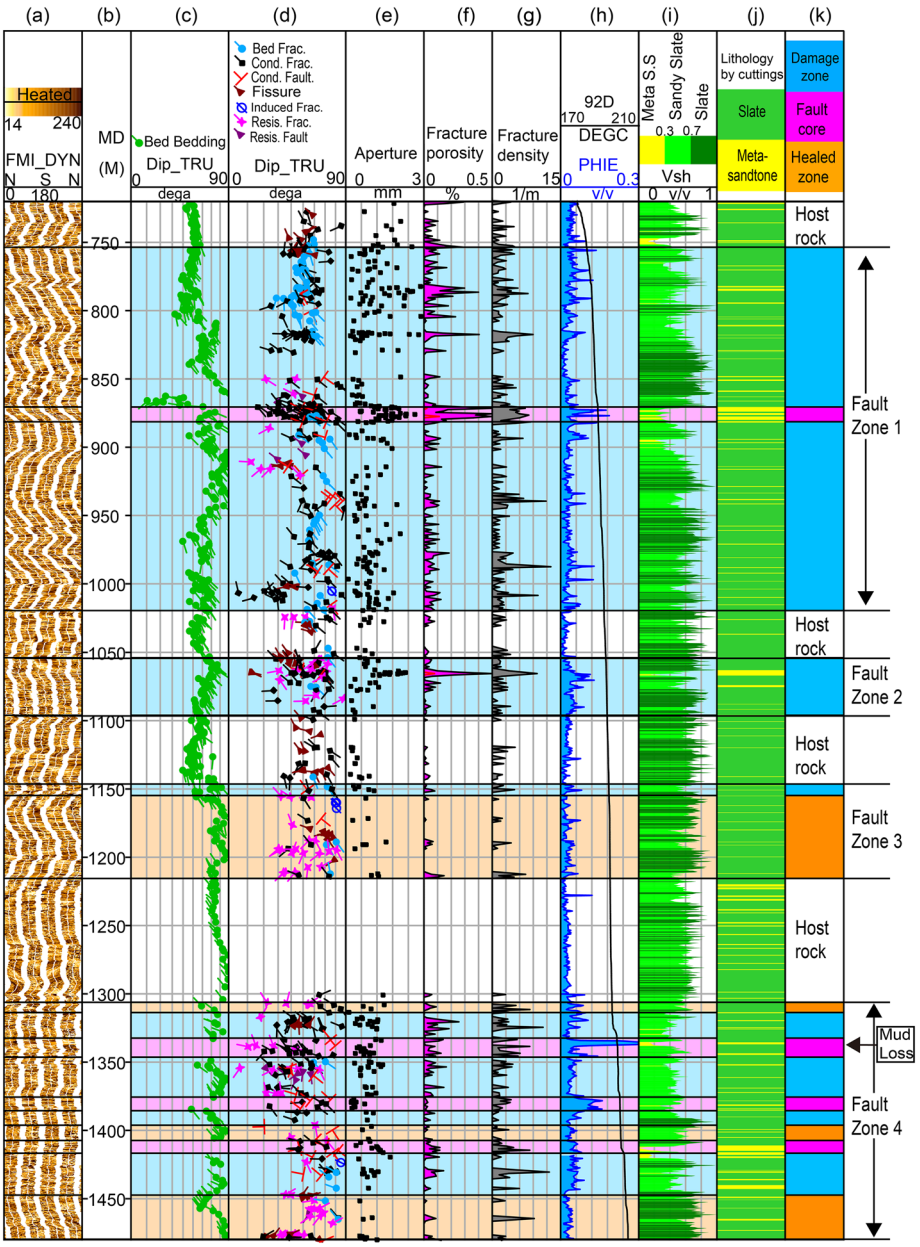

Fig. 5 Interpretation results of the FMI image. The interpretation results include the orientation of beddings, orientations of fracture planes, values of fracture aperture, fracture density, and fracture porosity. The 92D temperature log, *PHIE*, and lithology log are also shown for comparison with the FMI interpretation results

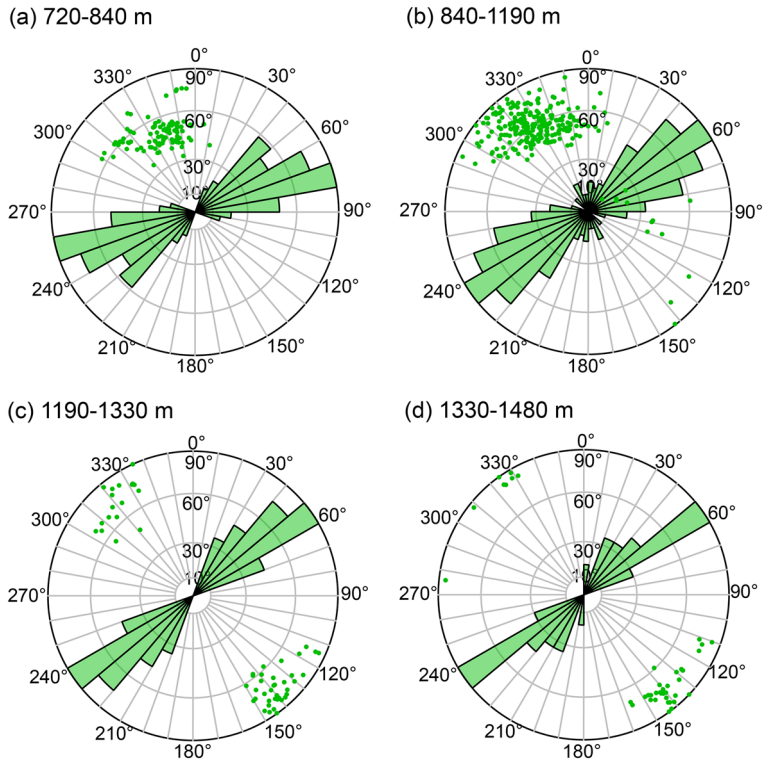

Fig. 6 Orientations of the bed boundaries. From 720 to 1480 m MD, the dominant strike of the strata rotated from N60–80°E (subfig.(a)) to N40–60°E (subfig. (b) to (c)), and the dominant dip direction rotated from the SE to the NW (subfig. (c) to (d)) near the well bottom

1) 720–840 m MD: N60–80°E/40–80°SE;
2) 840–1190 m MD: N50–70°E/50–90°SE;
3) 1190–1330 m MD: N40–60°E/60–90°SE to 60–90°NW; and
4) 1330–1480 m MD: N50–60°E/80–90°SE to 70–90°NW.

On the land surface in this area, the formation is mainly NE–SW trending and dips at a large angle to the SE. In the JT-4 well, the dominant attitudes of beds above 840 m MD are N60–80°E/40–80°SE similar to most formations in this region. The attitudes of formations below 840 m MD slowly rotate to N40–60°E/70–90°NW. At Jentse, mesoscale folds are developed only in conjunction with large fault zones. Therefore, herein, the beds are interpreted as being rotated by faulting mechanisms.

Image interpretations of fracture planes

Drilling-induced tensile fractures, four types of natural open fracture planes, and two types of natural sealed fractures were observed in the studied well interval. The strikes of the drilling-induced tensile fractures observed are mainly N40–50°E and the dips are mainly near vertical (Fig. 7). Borehole breakouts were rare and unclear on the FMI image within the studied well interval. Thus, borehole breakouts were not analyzed in this study.

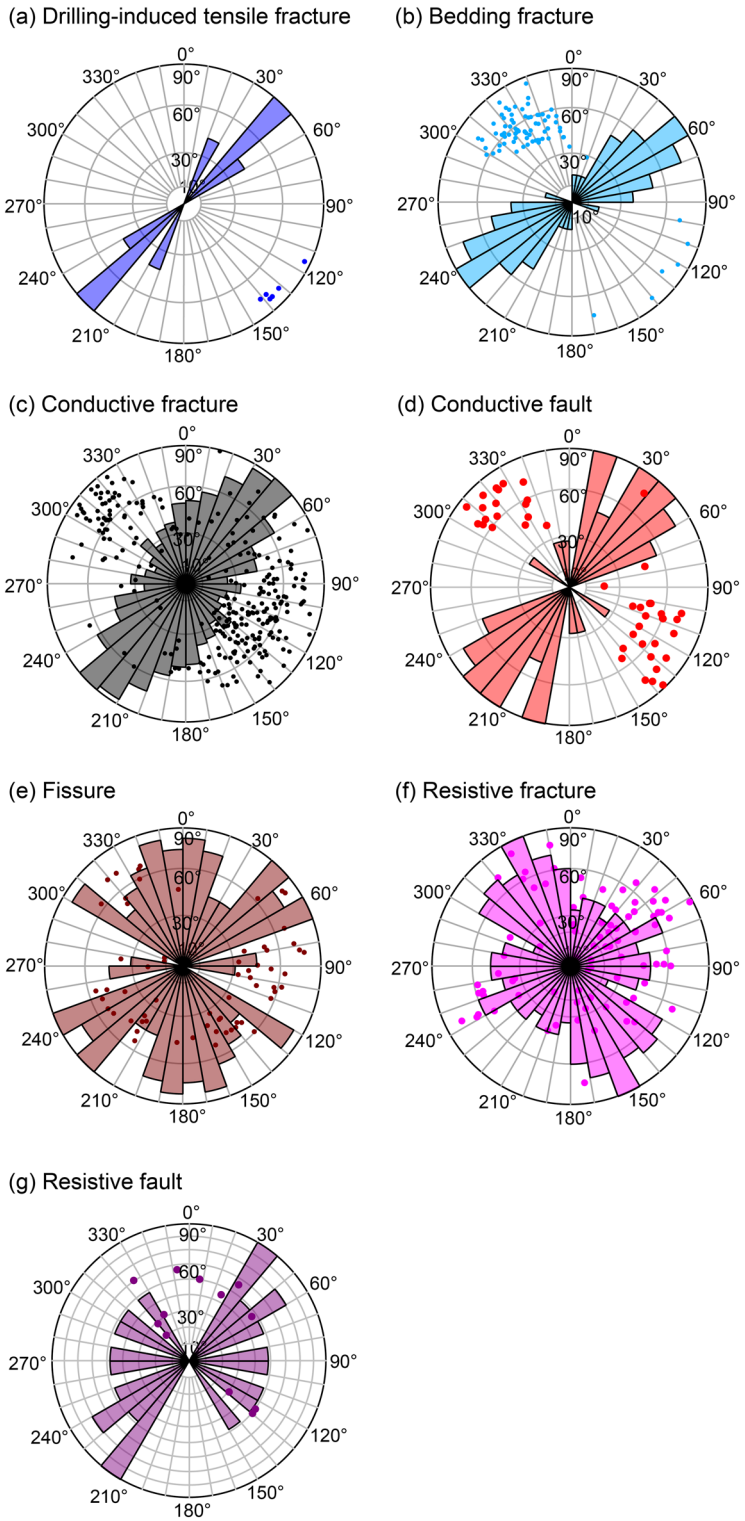

Fig. 7 Statistics of the orientations of different kinds of fracture planes, including drilling-induced tensile fractures (subfig(a)), naturalconductive fractures (subfig. (b) to (e)), and natural sealed fractures (subfig (f) and (g))

The four types of natural open fracture planes include bedding fractures, conductive fractures, conductive faults, and fissures. These four types of natural fracture planes all appear as dark-colored sinusoids in the FMI images. They are usually correlated with high *PHIE* and low *Vsh* values, denoting that most of the dark-colored fracture planes are open but not clay filled.

Bedding fracture planes were present at bed boundaries, which are also electrically conductive. Bedding fractures were usually wider and more irregular or distorted than bed boundary surfaces. The orientations of most of the bedding fractures are N50–70°E/50–80°SE (Fig. 7). Since the development of the bedding fracture planes can be controlled by weak bedding planes, this study separated them from other conductive fracture planes. With the exception of bedding fracture planes, most other conductive fractures strike parallel to their adjacent formation beds and dip toward the opposite direction of the dip of the adjacent formation beds (Figs. 7 and 8). Additionally, open fracture planes that show clear offsets between the two sides of the planes are defined as conductive fault planes in this study. The dominant strikes of the conductive fractures and conductive faults are mostly N30–50°E and the dips are 30–90° toward NW or SE (Fig. 7). Compared to the conductive fractures and faults, fissures have poorer continuity

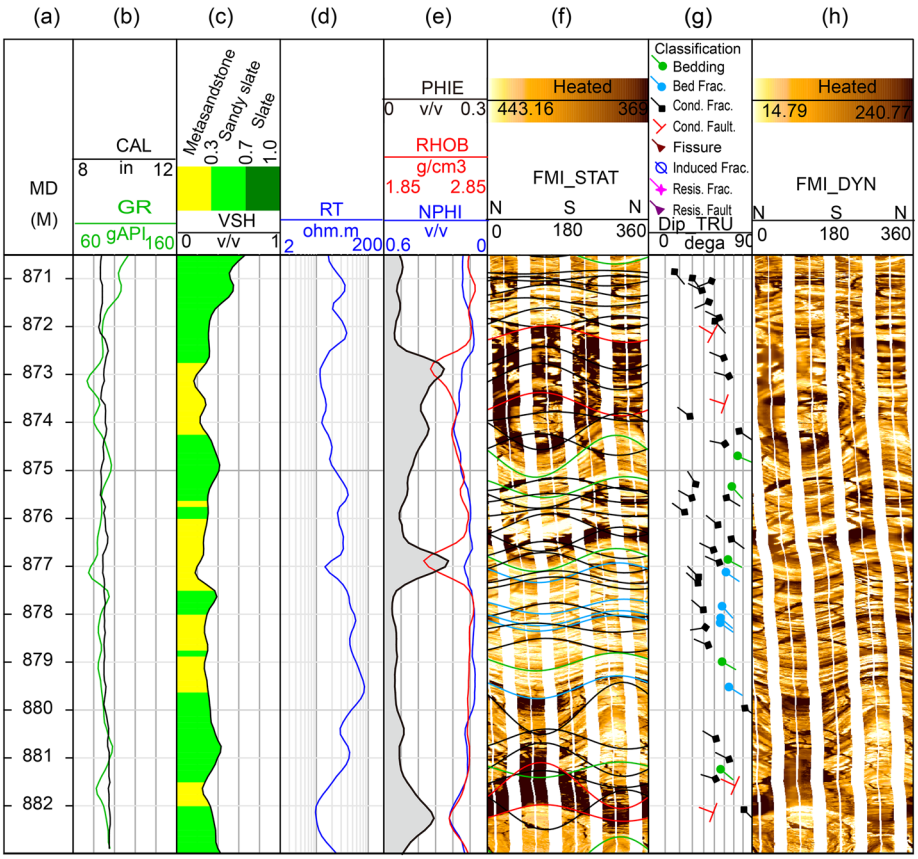

Fig. 8 Key geophysical logs and the FMI image of the 872–882 m MD fault core. The geophysical logs denote the lithology (*GR* and *Vsh* logs) and porosity (*PHIE*, *RHOB*, *NPHI*, and *RT* logs). The two most fractured intervals within the fault core are 872–874 and 881–882 m MD. These two intervals developed in the metasandstones (low *GR*) with high porosity (low *RT*, low *RHOB*, and high *NPHI* values). The attitude of the bounding fault planes at 872 and 882 m MD is around N40–50°E/45–55°NW

and weaker color contrasts to the background rock matrix. In contrast the other three types of open fractures with dominant orientations, the orientations of fissures were more widely distributed in the studied interval.

The two types of natural sealed fracture planes are resistive fracture planes and resistive fault planes. They appear as bright-colored sinusoids in the FMI image. In the FMI images, the sealed fracture planes are considerably thinner and less clear than the open fracture planes. The dominant orientations of the resistive fracture planes are NW–SE in strike and they dip toward NE and SW with low to high angles. Additionally, resistive fault planes have clear fault offsets and no dominant orientation (Fig. 7). Two most brecciated zones were identified in the study interval, which are the 872–882 m MD interval and the 1334–1346 m MD interval (Figs. 8 and 9). The characteristics of porous fault breccia are clear on the FMI image log in these two intervals.

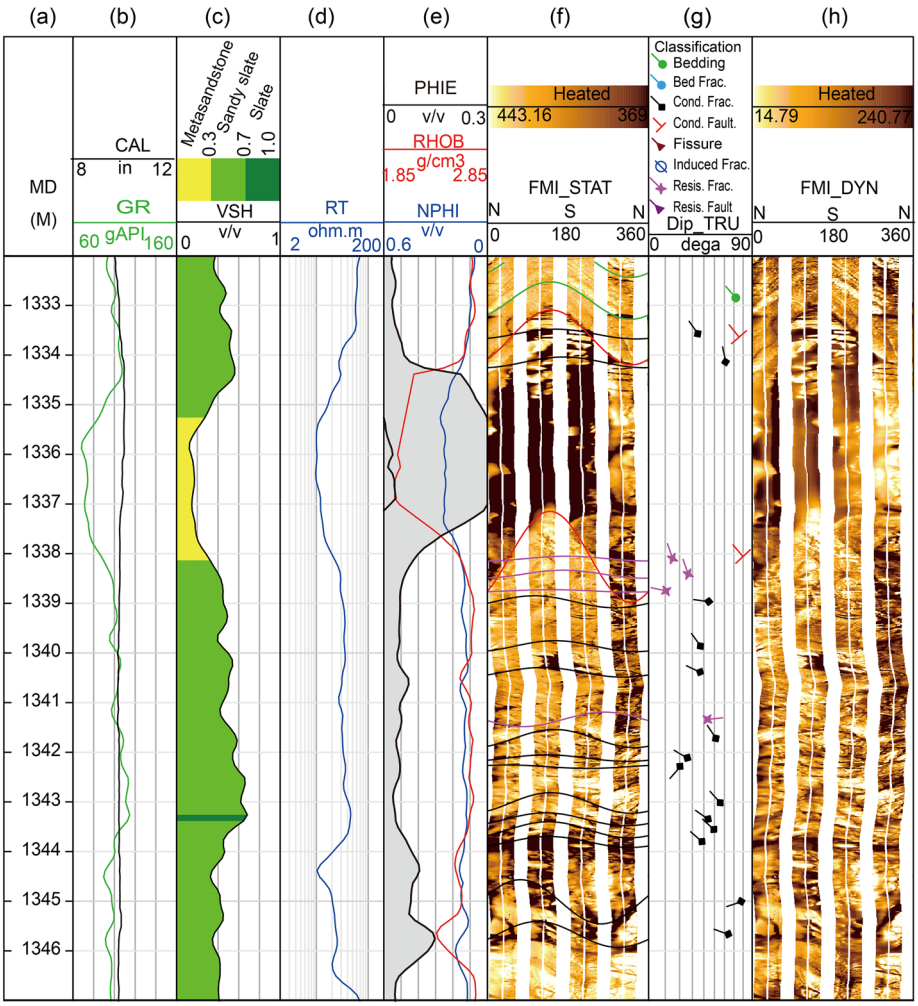

Fig. 9 Key geophysical logs and the FMI image of the 1334–1346 m MD fault core. The geophysical logs denote the lithology (*GR* and *Vsh* logs) and porosity (*PHIE*, *RHOB*, *NPHI*, and *RT* logs). The two most fractured intervals within the fault core are 1334–1339 and 1343–1346 m MD. The 1334–1339 m interval developed in the metasandstones (low *GR*) with extremely high porosity (low *RT*, low *RHOB*, and high *NPHI* values). This interval is the most permeable interval in the studied well section. The attitude of the bounding fault planes at 1334 and 1338 m MD is about N50E/75–80°NW

Summaries of values of open fracture density, fracture aperture, and fracture porosity

To determine the possible hydraulic potentials of open fracture planes, the fracture parameters of the four types of open fracture planes were analyzed. The density of the open fracture planes varied between 0 and 15 trace/m. The fracture aperture ranged from 0 to 3.0 mm, and the fracture porosity ranged from 0 to 0.5% (Fig. 5). The data show that the fracture intensity is unevenly distributed in the studied well section.

Log zonation results based on fracture characteristics

The locations and intervals of fault zones may be indicated by the following criteria:

1) Abrupt changes in bed orientations,
2) Appearance of breccia zones or fracture planes,
3) Values of fracture density, fracture aperture, and fracture porosity.

Based on the above criteria, four fault zones were classified. Each discrete fault zone is separated by intact host rocks (Fig. 5). The FMI image shows that the four fault zones have different internal structures. Three types of internal structures were identified. The fault cores comprise porous fault breccia. The fault damage zones exhibit a high density of open fracture planes. These two types of internal structures are porous and permeable. The third type is the healed zones, which comprise sealed fracture planes and sealed breccia zones (Fig. 5).

According to the zoning criteria, Fault Zone 1 (754–1021 m MD) comprises one fault core and two fault damage zones. Fault Zone 2 (1054–1096 m MD) comprises only one fault damage zone. Fault Zone 3 (1146–1215 m MD) comprises one short fault damage zone and one long healed zone. Fault Zone 4 (1305–1480 m MD) comprises three fault cores, four fault damage zones, and three healed zones (Fig. 5). Figure 10 displays the values of average *Vsh*, *PHIE*, fracture density, and fracture porosity of three kinds of internal structures within fault zones and host rock. The figure and summaries in Table 1 show that the average values of the faulted rocks are distinctly different from those of non-faulted rocks.

Discussion

Internal structures and characteristics of fault zones

This study confirmed the development of Fault Zones 1–4 in the studied well section by the abrupt tilting and rotation of the strata. Moreover, the fault zones are separated by intact host rock (Figs. 3 and 5). Based on the temperature log, geophysical log, and FMI borehole images, Zones 1, 2, and 4 have good permeability, while Zone 3 mainly comprises sealed fractures and should be an almost healed fault zone. Because Fault Zones 1–4 are in close proximity and have similar fracture characteristics, this study suggests that they constitute a major permeable fault system in the Jentse area.

As identified herein, there is one breccia zone in Fault Zone 1 and three breccia zones in Fault Zone 4. These breccia zones are classified as fault cores. The non-brecciated intervals containing fracture planes are categorized as damage zones. Fault zone 3 comprised few open fracture planes and mainly sealed fracture planes; therefore, Fault Zone

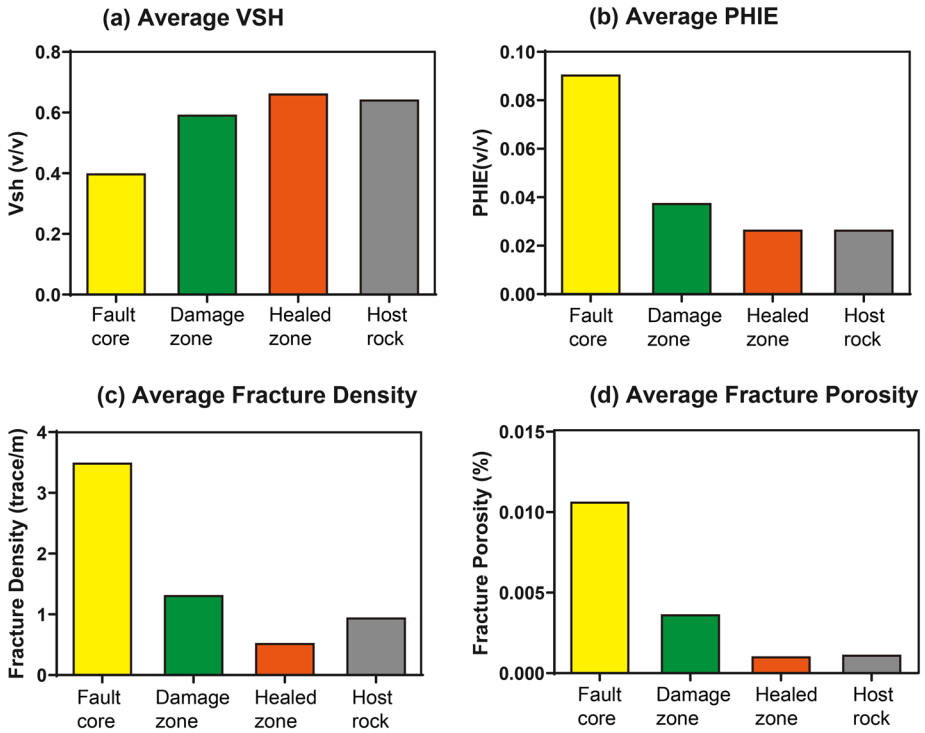

Fig. 10 Average *Vsh, PHIE*, fracture density, and fracture porosity values of the fault cores, fault damage zones, host rock, and healed zones. Fault cores are less shaly (subfig. (a)) and on an average comprise have high *PHIE* (subfig. (b)), high fracture density (subfig. (c)) and high fracture porosity (subfig. (d)). The healed zones and host rocks are tight comparing to fault cores and damage zones estimated by PHIE, fracture density, and fracture porosity

3 is considered a tight fault zone that the fractures are almost sealed by cements. Based on the temperature log and geophysical logs, the fault cores are the most permeable intervals of the fault zones followed by fault damage zones (Figs. 2 and 10).

Many low-resistivity (dark color) fractures were observed in the studied well interval. The low resistivity may indicate high porosity or the existence of electrically conductive clay minerals (Chen et al. 2021). Since low-resistivity fracture zones do not correspond to high *Vsh* (low *GR*) values (Figs. 3, 8 and 9), such low resistivity does not stem from the presence of conductive clay minerals but stems from the development of fracture porosity.

Because calcite and quartz are the most common minerals in the sealed fractures in the northern Central Range (Lu et al. 2018; Song and Lu 2019), the high resistance fractures were probably caused by calcite or quartz filling. Small amounts of calcite and quartz were observed in the cuttings of this well, further supporting the observations from the FMI borehole image.

Factors controlling the development of permeable fault zones

This study finds that fracture intensity in the studied well section is highly related to the corresponding lithology. Metasandstones tend to produce fault breccia, and the slates

Table 1 The summary of the average important log values of different fault zones, including each damage zone, fault core within the fault zones, and host rock between two fault zones

Zone name	Depth	Avg. *Vsh*	Avg. *PHIE*	Avg. fracture density
Unit	(m MD)	(%)	(%)	(1/m)
Fault zone 1	**754–1021**			
Damage zone	754–872	61.9	3.5	0.44
Fault core	***872–882***	***30.1***	***7.3***	***1.6***
Damage zone	882–1021	62.2	3.4	0.57
Host rock	1021–1054	68.9	1.6	0.42
Fault zone 2	**1054–1096**			
Damage zone	1054–1096	66.9	4.6	0.76
Host rock	1096–1146	71.2	2.4	0.29
Fault zone 3	**1146–1215**			
Damage zone	1146–1154	61.5	3.3	045
Healed zone	1154–1215	68.6	2.4	0.87
Host rock	1215–1305	64.3	2.4	0.19
Fault zone 4	**1305–1480**			
Healed zone	1305–1314	56.5	5	0.36
Damage zone	1314–1334	41.8	4.3	1.08
Fault core	***1334–1346***	***40.6***	***12.7***	***1.33***
Damage zone	1346–1375	44.8	4.3	1.24
Fault core	***1375–1385***	***48***	***11.2***	***1.06***
Damage zone	1385–1394	56.1	5.9	1.58
Healed zone	1394–1407	61	3.6	0.63
Fault core	***1407–1417***	***40.4***	***5.4***	***0.68***
Damage zone	1417–1447	50.4	5	0.38
Healed zone	1447–1480	71.4	2.9	0.36

It shows that fault cores usually have lower average Vsh, higher PHIE, and higher fracture density

We modify the Damage zone and Healed zone to be normal fonts in order to be clearer

Bold normal fonts are the interval of each fault zone

Bold Italic fonts are the interval of fault core within different fault zones

with higher shale volumes tend to produce fracture planes. Not only in Jentse, other studies have shown similar results (i.e., Bense et al. 2013; Sibson 1994; Wallis et al. 2012).

This study assumes that to maintain permeability of the fractures, this area needs to be in a critically stressed tectonic environment. The open fractures should have a tendency to move. The reason is that open fractures could be supported and maintained by the tectonic stresses in a critically stressed tectonic environment (Barton and Zoback 2002; Jolie et al. 2021; Zoback 2007). However, long fault displacements may eventually cause permeable fault breccias to become thick impermeable fault gauges (Gray et al. 2005; Holland et al. 2006; Micarelli et al. 2006), which are not observed in the studied interval. Thus, recent short fault displacement may be a reason for the presence of permeable fault cores in Fault Zones 1, 2, and 4.

Unlike Fault Zones 1, 2, and 4, the Fault Zone 3 would be an impermeable fault zone. Although it exhibits abrupt bedding rotations and fracture developments, most of the fractures therein are impermeable and exhibit high resistivity (Fig. 3). Geophysical logs also indicate that the petrophysical properties of the most parts of Fault Zone 3 are similar to those of the intact host rock. Thus, this study believes that the permeability of the most parts of Fault Zone 3, an almost healed fault zone, should be as low as the intact host rock of this area.

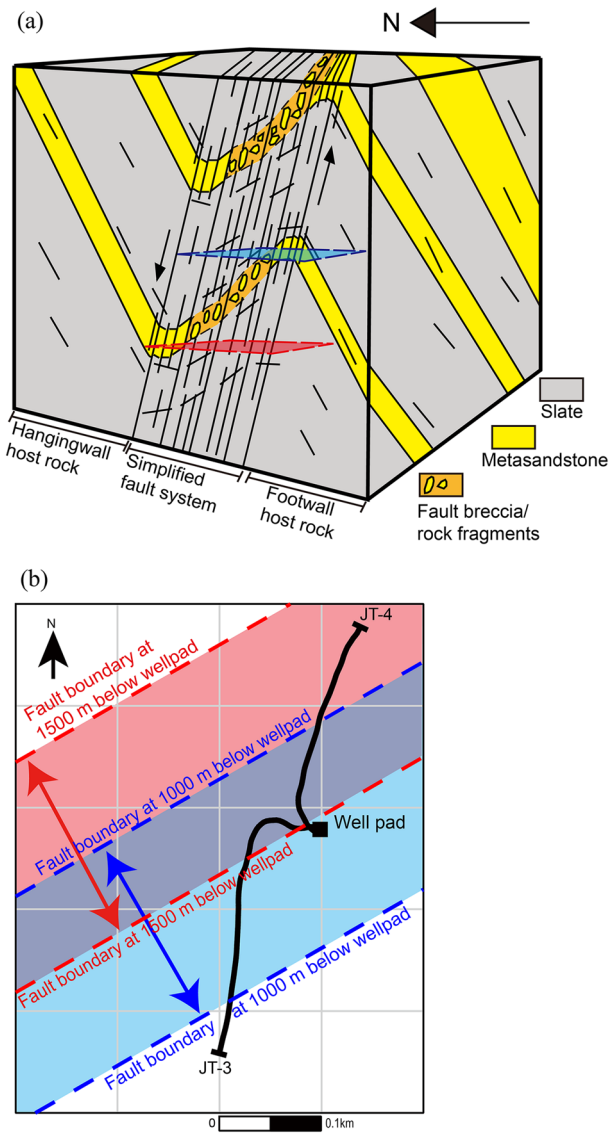

Fig. 11 Subfig (**a**) shows the conceptual model of the major permeable fault system in Jentse. By fault dragging, the beds rotated to be parallel to the fault system. The metasandstone within the fault system tend to break into rock fragments. The slates tend to develop fracture planes. Subfig (**b**) shows the orientation and width of the fault system. The areas between the two blue and red dashed lines are the possible location of the fault system at 1000 and 1500 m below wellpad, respectively (the elevation of the well pad is 550 m above sea level). The fault system shifts to the northwest from shallow to deep. The conceptual locations of blue and red areas in subfig (**b**) are also showed in subfig (**a**)

Structural heterogeneity within fault zones

The Jentse geothermal area is composed of thin brittle metasandstones interlayered with thick slate beds. In this area, the faults and strata are cross-cutting. Therefore, the highly fractured brittle metasandstone beds could be truncated by slate and deformed into discrete disc- or pipe-shaped porous rock bodies (Fig. 11). Such structural heterogeneity stems from a combination of lithological and tectonic factors. We suggest good fracture porosity and permeability is not present over the entire fault system, but there is strong heterogeneity. When the geothermal well penetrates a fault system with good fracture porosity, it is possible that the fluid flow within the fault system would be blocked by tight rock bodies in a distance from the borehole and a stable production rate cannot be maintained.

The deflections of the temperature logs

This study attempted to observe whether the temperature logs reasonably reflect the fault development. Generally, the borehole temperature represents the temperature of its lateral strata in the vicinity of the borehole. However, shortly after the end of drilling, the well temperature generally steeply increases at 25–50 m above the bottom of the well because of the upward heat transfer from the strata below the well bottom. After shutting in the well for 92 days, the 92D log shows the high temperature near the bottom of the well disappeared indicating the temperature equilibrium near the bottom of the borehole (Fig. 2).

The formation temperature near the borehole decreased due to the drilled mud circulation during the drilling. In the JT-4 well, the 34H, 51H and 64H logs show that the temperature increases through time and that some temperature fluctuations are consistent with the locations of the open fractures. Such small temperature spikes may stem from small-scale circulation adjacent to the borehole, and these spikes may not maintain in the long-term temperature logs (Vidal et al. 2019).

The 1334–1346 m MD fault core of Fault Zone 4 has the most significant temperature anomalies on the four different temperature logs. The temperature anomalies are all negative deflections on the 34H, 51H, and 64H logs in this major fault core and are a positive deflection in the 92D log. The magnitude and the directions of deflections denote the combined responses of the flow rate and fluid temperature into the borehole from the fault zones (Vidal et al. 2019). Negative temperature anomalies imply that colder fluid flows within the fault zone. The cold fluids may be the drilling mud filtrates or the formation fluid from colder formations. Positive temperature anomalies mean that hotter water flows into the borehole from deep strata along the planer fault zone.

The negative anomalies of 34H, 51H, and 64H temperature logs may suggest that water from shallow and cold strata flowed into the 1334–1346 m MD fault core during the period of tens of hours after the end of well drilling. Another reason for the negative anomalies may be there were huge volume of cold drilling mud filtrate flowed into the fault zone during drilling. It took longer time for the drilling mud filtrate to heat up because its higher heat capacity comparing to the formation rocks.

After 92 days from the end of well drilling, the geothermal water from deep and hot strata gradually flowed into the borehole along the 1334–1346 m MD fault core shown in the 92D log. The study results denote that the deflections of the temperature curves

may to some extent reflect the permeability of fault zones in this region. The temperature value anomalies in the 1334–1346 m MD denote that the flow direction of geothermal fluid would change within a few tens of days in highly permeable zones.

Characteristics of the permeability fault system in the Jentse area

Possible location of the permeability fault system

The identified Fault Zones 1–4 are considered to be one major regional fault system due to their close proximity and similar nature. For further geothermal exploration, this study used the dragging directions of the strata and the orientations of the open fractures to determine the possible subsurface attitude of the fault system.

The attitude of the strata between 840 and 1480 m MD of the JT-4 well is clearly rotated by fault dragging. According to previous studies, the attitudes of strata adjacent to or within the fault zone tend to be parallel or subparallel to the fault zones after fault dragging (Bengtson 1981; Hesthammer and Fossen 1998; Schlumberger 1986). The conceptual idea is shown in Fig. 11. This study concludes that the attitude of strata between 840 and 1480 m MD, N50–70°E/70–80°NW, should be approximately parallel to the permeable fault system encountered by the JT-4 well. Additionally, the attitude of the fault system encountered in the JT-3 well is also N50–70°E/70–80°NW (Chen et al. 2021). By integrating the independent results of the JT-3 and JT-4 wells, the two wells were drilled to encounter the same subsurface fault system of the Jentse geothermal area. The strike of this fault system subsurface is parallel to the "I" and "K" faults exposed on the surface (Fig. 1). However, whether the subsurface fault system is connected to the "I" or "K" fault at the surface still needs to be confirmed.

The true thickness of the fault system encountered in a borehole can be calculated based on the apparent thickness and attitude of the fault system as well as the borehole trajectory (Tearpock et al. 2003). Since the wellbore trajectory intersects the fault system at a small angle, the true width of each fault zone is only 1/3–1/4 the apparent thickness penetrated in the JT-4 well. The interval of the main fault system in the JT-4 well is 754–1480 m MD, and the true width of the fault system in this well section would be approximately 200 m by calculation. Based on the results of this study and Chen et al. (2021), the possible location of the permeable fault system subsurface is plotted in Fig. 11. However, the horizontal continuation of the permeable fault system and the changes of its internal structures need to be verified in future studies.

In addition, because there are many faults and small folds in Jentse, it is still difficult to fully reveal the subsurface structure only by the JT-3 and JT-4 well data. Furthermore, there is still a lack of credible geophysical data in this area. In the future, the integration of geophysical data, surface geological surveys, and well data are needed to establish a reliable 3-D subsurface geothermal structural model.

Relation among open fractures, permeable fault system, and regional tectonics

Generally, the orientation of the drilling-induced tensile fractures coincides with the orientation of the maximum horizontal principal stresses in vertical wells or wells with small deviation angles (Zoback et al. 2003). This study examined the orientations of drilling-induced tensile fractures in the 720–1480 m MD section of the JT-4 well and

determined that the strike of the fractures is mainly N40–50°E and the dips are nearly vertical. Based on the orientation of the drilling-induced tensile fractures, the orientation of the maximum horizontal principal stress should also be NE–SW. The direction of the maximum horizontal principal stress derived herein is similar to the results of GPS studies, other geophysical studies, and well data in the northern Central Range (Chen et al. 2021; Hsu et al. 2009; Huang et al. 2012; Yeh et al. 2013). The consistency of the direction of the open faults and the direction of the local tectonic stress field is in agreement with the assumption that the open fracture can usually be maintained in a critically stressed state. (Zoback 2007). This phenomenon has been observed in hydrocarbon and geothermal reservoirs (Hennings et al. 2012; Jolie et al. 2015).

Even though this study and other studies (i.e., Chen et al. 2021; Hsu et al. 2009; Huang et al. 2012; Yeh et al. 2013) suggest that the northern Central Range had been affected by recent regional rifting extending from northeastern edge of Taiwan, most of the NE–SW trending faults found in Jentse were formed by the early stage of tectonic collision. These faults have poorly permeable internal structures. This study suggests that younger faults, which are the result of recent regional rifting, would be more permeable and productive for geothermal fluids in Jentse. Based on the study results, future geothermal exploration in this area should focus on fault zones that have tended to be critical stressed, such as the Fault Zone 1 and 4 found in this study, in recent geological time.

Conclusion

This study analyzed geophysical logs and FMI borehole images between 720 and 1475 m MD of the JT-4 well to determine the characteristics of fault zones and fault-related fractures in the Jentse geothermal area. The orientations of the open fractures and drilling-induced tensile fractures identified in JT-4 well are similar and strongly concentrated toward N50–70°E. In addition, analysis of the formation faulting in the JT-3 and JT-4 wells indicates that the main permeable fault system at Jentse is a normal fault oriented N50–70°E/70–80°NW. The similar orientations of fractures and the fault system suggest that permeable fractures and geothermal system developments in northeastern Taiwan is related to the present-day tectonic extension caused by the Okinawa Trough rifting offshore the northeastern Taiwan.

Notably, the permeable zones in the studied well intervals tend to concentrate in Fault Zones 1, 2, and 4. Fault Zone 3 is a fault zone that almost healed and is devoid of high porosity and permeability. The internal structures of the permeable fault zones comprise fault cores and damage zones. Fault cores are primarily fault breccias, and fault damage zones comprise numerous fracture planes. Based on the integration of borehole temperature, geophysical logs, and borehole images, the most permeable interval is the 1433–1446 m MD fault breccia zone in Fault Zone 4. The healed zones comprise sealed fracture structures are non-permeable and should be of the same quality as intact host rocks.

The geophysical logs acquired herein could be used to separate metasandstone and slate. Since no apparent hydrothermal alteration was observed, only small amounts of clay minerals formed in the fault zones. Because there are few altered clay minerals, the metasandstone and slate could be separated by the *GR* log. If the rocks are highly

fracturing, other geophysical logs excluding the *GR* log would exhibit certain responses indicating higher porosity. The understanding of the subsurface permeable fault properties ascertained in this study will be useful for future geothermal exploration and development in northeastern Taiwan.

Acknowledgements
We would like to thank the editor and two reviewers (Dr. Mochamad Nukman and Dr. Michal Kruszewski) for their criticisms and very constructive comments, which helped to improve the manuscript. This research used materials and software provided by the Exploration & Production Business Division, CPC Corporation Taiwan. The research was supported by the Taiwan ROC (Republic of China) Ministry of Science and Technology (MOST 110-2116-M-008-002-MY2 and NSTC 112-2119-M-213-001) and Earthquake-Disaster & Risk Evaluation and Management Center, "EDREaM", from the Ministry of Education (MOE) to Li-Wei Kuo. Thanks to Dr. Sheng-Rong Song for the discussion.

Author contributions
B-CC, TP, L-WK wrote the paper; B-CC conceived the present idea; B-CC and TP analyzed the data; B-CC and TP contributed materials and analysis tools; all the authors part to the discussion. B-CC coordinated the study.

Funding
Funding the research was supported by the Taiwan ROC (Republic of China) Ministry of Science and Technology (MOST 110-2116-M-008–002-MY2 and NSTC 112-2119-M-213-001) and Earthquake-Disaster & Risk Evaluation and Management Center (E-DREaM) from the Ministry of Education (MOE) to Li-Wei Kuo.

Availability of data and materials
All data used in this study are available by contacting the first author B.-C. Chen (cpc050881 + Bill@gmail.com).

Declarations

Competing interests
The authors have no competing interests to declare that are relevant to the content of this article.

Received: 10 December 2022 Accepted: 23 July 2023
Published online: 05 August 2023

References

Ameen MS. Fracture and in-situ stress patterns and impact on performance in the Khuff structural prospects, eastern offshore Saudi Arabia. Mar Pet Geol. 2014;50:166–84. https://doi.org/10.1016/j.marpetgeo.2013.10.004.
Angelier J, Chang TY, Hu JC, Chang CP, Siame L, Lee JC, Deffontaines B, Chu HT, Lu CY. Does extrusion occur at both tips of the Taiwan collision belt? Insights from active deformation studies in the Ilan Plain and Pingtung Plain regions. Tectonophysics. 2009;466(3–4):356–76. https://doi.org/10.1016/j.tecto.2007.11.015.
Barton CA, Zoback MD. Discrimination of natural fractures from drilling-induced wellbore failures in wellbore image data—implications for reservoir permeability. SPE Reservoir Eval Eng. 2002;5(03):249–54. https://doi.org/10.2118/78599-PA.
Bengtson CA. Statistical curvature analysis techniques for structural interpretation of dipmeter data. Am Asso Petrol Geol Bull. 1981;65(2):312–32. https://doi.org/10.1306/2f9197c9-16ce-11d7-8645000102c1865d.
Bense VF, Gleeson T, Loveless SE, Bour O, Scibek J. Fault zone hydrogeology. Earth Sci Rev. 2013;127:171–92. https://doi.org/10.1016/j.earscirev.2013.09.008.
Caine JS, Evans JP, Forster CB. Fault zone architecture and permeability structure. Geology. 1996;24(11):1025–8.
Chang YK, Lee HS, Yang JH, Wu GH, Lee JY. Geological Report of the Jentse and Tuchang Geothermal area, Ilan. CPC Corporation Taiwan. 1986. p. 24.
Chang PY, Lo W, Song SR, Ho KR, Wu CS, Chen CS, Lai YC, Chen HF, Lu HY. Evaluating the Chingshui geothermal reservoir in northeast Taiwan with a 3D integrated geophysical visualization model. Geothermics. 2014;50:91–100. https://doi.org/10.1016/j.geothermics.2013.09.014.
Chang PY, Ho GR, Chen CC, Hsu HL, Chen CS, Yeh EC. An analysis of the subsurface fault systems with audio-magnetotelluric surveys in the western Ilan Plain of NE Taiwan. Terr Atmos Ocean Sci. 2020;31(5):551–64. https://doi.org/10.3319/TAO.2020.02.17.01.
Chen CH. Chemical characteristics of thermal waters in the Central Range of Taiwan, R.O.C. Chem Geol. 1985;49(1–3):303–17. https://doi.org/10.1016/0009-2541(85)90163-9.
Chen CT, Chan YC, Beyssac O, Lu CY, Chen YG, Malavieille J, Kidder SB, Sun HC. Thermal history of the northern Taiwanese slate belt and implications for wedge growth during the Neogene arc-continent collision. Tectonics. 2019;38(9):3335–50. https://doi.org/10.1029/2019TC005604.
Chen BC, Perdana T, Kuo LW. Fluid flow and fault-related subsurface fractures in slate and metasandstone formations: a case study of the Jentse Geothermal Area, Taiwan. Geothermics. 2021;89(300):101986. https://doi.org/10.1016/j.geothermics.2020.101986.
Chiang CW, Hsu HL, Chen CC. An investigation of the 3D electrical resistivity structure in the Chingshui geothermal area, NE Taiwan. Terr Atmos Ocean Sci. 2015;26(3):269–81. https://doi.org/10.3319/TAO.2014.12.09.01(T).
CPC. CPC-JT-2T well drilling report. CPC Corporation Taiwan. 1984. p. 55.
Crain PE. Crain's petrophysical handbook. 2023. https://spec2000.net/index.htm.

Faulkner DR, Jackson CAL, Lunn RJ, Schlische RW, Shipton ZK, Wibberley CAJ, Withjack MO. A review of recent developments concerning the structure, mechanics and fluid flow properties of fault zones. J Struct Geol. 2010;32(11):1557–75. https://doi.org/10.1016/j.jsg.2010.06.009.

Gray MB, Stamatakos JA, Ferrill DA, Evans MA. Fault-zone deformation in welded tuffs at Yucca Mountain, Nevada, USA. J Struct Geol. 2005;27(10):1873–91. https://doi.org/10.1016/j.jsg.2005.01.018.

Hamahashi M, Hamada Y, Yamaguchi A, Kimura G, Fukuchi R, Saito S, Kameda J, Kitamura Y, Fujimoto K, Hashimoto Y. Multiple damage zone structure of an exhumed seismogenic megasplay fault in a subduction zone—a study from the Nobeoka Thrust Drilling Project. Earth Planets Space. 2015;67(1):1–21. https://doi.org/10.1186/s40623-015-0186-2.

Hennings P, Allwardt P, Paul P, Zahm C, Reid R, Alley H, Kirschner R, Lee B, Hough E. Relationship between fractures, fault-zones, stress, and reservoir productivity in the Suban gas field, Sumatra, Indonesia. AAPG Bull. 2012;96(4):753–72. https://doi.org/10.1306/08161109084.

Hesthammer J, Fossen H. The use of dipmeter data to constrain the structural geology of the Gullfaks Field, northern North Sea. Mar Pet Geol. 1998;15(6):549–73. https://doi.org/10.1016/S0264-8172(98)00028-2.

Ho GR, Chang PY, Lo W, Liu CM, Song SR. New evidence of regional geological structures inferred from reprocessing and resistivity data interpretation in the Chingshui-Sanshing-Hanchi area of Southwestern Ilan County, NE Taiwan. Terr Atmos Ocean Sci. 2014;25(4):491–504. https://doi.org/10.3319/TAO.2014.01.24.01(TT).

Holland M, Urai JL, van derZee W, Stanjek H, Konstanty J. Fault gouge evolution in highly overconsolidated claystones. J Struct Geol. 2006;28(2):323–32. https://doi.org/10.1016/j.jsg.2005.10.005.

Houwers ME, Heijnen LJ, BeckerA, Rijkers R. A workflow for the estimation of fault zone permeability for geothermal production a general model applied on the Roer Valley Graben in the Netherlands. In: Proceedings World Geothermal Congress 2015, April, 9. 2015.

Hsiao PT, Chiang SC. Geology and geothermal system of the Chingshui-Tuchang geothermal area, Ilan, Taiwan. Pet Geol Taiwan. 1979;16:205–13.

Hsu YJ, Yu SB, Simons M, Kuo LC, Chen HY. Interseismic crustal deformation in the Taiwan plate boundary zone revealed by GPS observations, seismicity, and earthquake focal mechanisms. Tectonophysics. 2009;479(1–2):4–18. https://doi.org/10.1016/j.tecto.2008.11.016.

Huang HH, Shyu JBH, Wu YM, Chang CH, Chen YG. Seismotectonics of northeastern Taiwan: kinematics of the transition from waning collision to subduction and postcollisional extension. J Geophys Res Solid Earth. 2012;117(1):1–13. https://doi.org/10.1029/2011JB008852.

Huang YH, Liu HL, Song SR, Chen HF. An ideal geothermometer in slate formation: a case from the Chingshui geothermal field, Taiwan. Geothermics. 2018. https://doi.org/10.1016/j.geothermics.2017.11.002.

Jarzyna JA, Baudzis S, Janowski M, Puskarczyk E. Geothermal resources recognition and characterization on the basis of well logging and petrophysical laboratory data, polish case studies. Energies. 2021. https://doi.org/10.3390/en14040850.

Jeppson TN, Bradbury KK, Evans JP. Geophysical properties within the San Andreas Fault Zone at the San Andreas Fault Observatory at Depth and their relationships to rock properties and fault zone structure. J Geophy Res Solid Earth. 2010;115(12):1–20. https://doi.org/10.1029/2010JB007563.

Jolie E, Moeck I, Faulds JE. Quantitative structural-geological exploration of fault-controlled geothermal systems—a case study from the Basin-and-Range Province, Nevada (USA). Geothermics. 2015;54:54–67. https://doi.org/10.1016/j.geothermics.2014.10.003.

Jolie E, Scott S, Faulds J, Chambefort I, Axelsson G, Gutiérrez-Negrín LC, Regenspurg S, Ziegler M, Ayling B, Richter A, Zemedkun MT. Geological controls on geothermal resources for power generation. Nat Rev Earth Environ. 2021;2(5):324–39. https://doi.org/10.1038/s43017-021-00154-y.

Kuo LW, Song SR, Yeh EC, Chen HF. Clay mineral anomalies in the fault zone of the Chelungpu Fault, Taiwan, and their implication. Geophys Res Lett. 2009;36:L18306. https://doi.org/10.1029/2009GL039269.

Kuo LW, Li H, Smith SAF, di Toro G, Suppe J, Song SR, Nielsen S, Sheu HS, Si J. Gouge graphitization and dynamic fault weakening during the 2008 Mw 7.9 Wenchuan earthquake. Geology. 2014. https://doi.org/10.1130/G34862.1.

Kuo LW, di Felice F, Spagnuolo E, di Toro G, Song SR, Aretusini S, Li H, Suppe J, Si J, Wen CY. Fault gouge graphitization as evidence of past seismic slip. Geology. 2017. https://doi.org/10.1130/G39295.1.

Lai KY, Chen YG, Wu YM, Avouac JP, Kuo YT, Wang Y, Chang CH, Lin KC. The 2005 Ilan earthquake doublet and seismic crisis in northeastern Taiwan: evidence for dyke intrusion associated with on-land propagation of the Okinawa Trough. Geophys J Int. 2009;179(2):678–86. https://doi.org/10.1111/j.1365-246X.2009.04307.x.

Lee HS, Lee JY. Subsurface geological report of the CPC-JT-1T geothermal well in the Jentse geothermal district I Lan. CPC Corporation Taiwan. 1983. p. 19.

Lee JC, Angelier J, Chu HT. Polyphase history and kinematics of a complex major fault zone in the northern Taiwan mountain belt: the Lishan Fault. Tectonophysics. 1997;274(1–3):97–115. https://doi.org/10.1016/S0040-1951(96)00300-9.

Li D, Huang L, Zheng Y, Li Y, Wannamaker P, Moore J. Feasibility of source-free DAS logging for next-generation borehole imaging. Sci Rep. 2022. https://doi.org/10.1038/s41598-022-16027-3.

Lin CH. Thermal modeling of continental subduction and exhumation constrained by heat flow and seismicity in Taiwan. Tectonophysics. 2000;324(3):189–201. https://doi.org/10.1016/S0040-1951(00)00117-7.

Lin CW, Lin WH. Explanatory text of the geologic map of Taiwan Sanshin, Sheet 15, Central Geological Survey. Taiwan: MOEA; 1995.

Liotta D, Brogi A, Ruggieri G, Zucchi M. Fossil vs. active geothermal systems: a field and laboratory method to disclose the relationships between geothermal fluid flow and geological structures at depth. Energies. 2021. https://doi.org/10.3390/en14040933.

Liu CM, Song SR, Kuo CH. Silica geothermometry applications in the Taiwan orogenic belt. Terr Atmos Ocean Sci. 2015;26(4):387–96. https://doi.org/10.3319/TAO.2015.02.09.01(TT).

Lu YC, Song SR, Wang PL, Wu CC, Mii HS, MacDonald J, Shen CC, John CM. Magmatic-like fluid source of the Chingshui geothermal field, NE Taiwan evidenced by carbonate clumped-isotope paleothermometry. J Asian Earth Sci. 2017;149:124–33. https://doi.org/10.1016/j.jseaes.2017.03.004.

Lu YC, Song SR, Taguchi S, Wang PL, Yeh EC, Lin YJ, MacDonald J, John CM. Evolution of hot fluids in the Chingshui geothermal field inferred from crystal morphology and geochemical vein data. Geothermics. 2018;74(June):305–18. https://doi.org/10.1016/j.geothermics.2017.11.016.
Lu YC, Song SR, Lin PH, Taguchi S, Wang C, Lai YM, Peng TR, Lee HF. Thermal fluid changes after operating a geothermal system: a case study of the Chingshui geothermal field, Taiwan. Geothermics. 2020. https://doi.org/10.1016/j.geothermics.2020.101878.
Luthi SM, Souhaite P. Fracture apertures from electrical borehole scans. Geophysics Doi. 1990;10(1190/1):1442896.
Lyu W, Zeng L, Zhang B, Miao F, Lyu P, Dong S. Influence of natural fractures on gas accumulation in the Upper Triassic tight gas sandstones in the northwestern Sichuan Basin, China. Mar Pet Geol. 2017;83:60–72. https://doi.org/10.1016/j.marpetgeo.2017.03.004.
Micarelli L, Benedicto A, Wibberley CAJ. Structural evolution and permeability of normal fault zones in highly porous carbonate rocks. J Struct Geol. 2006;28(7):1214–27. https://doi.org/10.1016/j.jsg.2006.03.036.
Moeck IS. Catalog of geothermal play types based on geologic controls. Renew Sustain Energy Rev. 2014;37:867–82. https://doi.org/10.1016/j.rser.2014.05.032.
Peska P, Zoback MD. Compressive and tensile failure of inclined well bores and determination of in situ stress and rock strength. J Geophys Res. 1995. https://doi.org/10.1029/95jb00319.
Priest SD. Discontinuity analysis for rock engineering. London: Springer; 1993. https://doi.org/10.1007/978-94-011-1498-1.
Rowland JV, Sibson RH. Structural controls on hydrothermal flow in a segmented rift system, Taupo Volcanic Zone, New Zealand. Geofluids. 2004;4(4):259–83. https://doi.org/10.1111/j.1468-8123.2004.00091.x.
Schlumberger. Dipmeter interpretation fundamentals. New York: Schlumberger Ltd.; 1986. p. 76.
Schlumberger. Techlog wellbore imaging user manual. 2015.
Shen TT, Liu TK, Huang SY, Hsieh PS, Wu CY. Post-collisional exhumation and geotherm pattern in northern Tananao Complex, northeastern Taiwan. Terr Atmos Ocean Sci. 2020;31(4):369–81. https://doi.org/10.3319/TAO.2019.04.06.01.
Shyu JBH, Sieh K, Chen YG, Liu CS. Neotectonic architecture of Taiwan and its implications for future large earthquakes. J Geophys Res Solid Earth. 2005;110(8):1–33. https://doi.org/10.1029/2004JB003251.
Sibson RH. Crustal stress, faulting and fluid flow. Geol Soc Spec Publ. 1994. https://doi.org/10.1144/GSL.SP.1994.078.01.07.
Song S-R, Lu Y-C. Geothermal explorations on the slate formation of Taiwan. In: Ismail BI, editor. Renewable geothermal energy explorations. London: IntechOpen; 2019. https://doi.org/10.5772/intechopen.81157.
Su FC. Resistivity survey in the Chingshui prospect, Ilan, Taiwan. Petrol Geol Taiwan. 1978;16:255–64.
Su Z, Hu JC, Wang E, Li Y, Yang Y, Wang PL. Monitoring interseismic activity on the Ilan Plain (NE Taiwan) using Small Baseline PS-InSAR, GPS and leveling measurements: partitioning from arc-continent collision and backarc extension. Geophys J Int. 2018;212(1):264–83. https://doi.org/10.1093/gji/ggx394.
Taguchi S, Nakamura M. Subsurface thermal structure of the Hatchobaru geothermal system, Japan, determined by fluid inclusion study. Geochem J. 1991;25(4):301–14. https://doi.org/10.2343/geochemj.25.301.
Tearpock DJ, Bischke RE, Walker LG. Applied subsurface geological mapping with structural methods. Upper Saddle River: Prentice Hall PTR; 2003.
Teng LS. Extensional collapse of the northern Taiwan mountain belt. Geology. 1996;24(10):949–52. https://doi.org/10.1130/0091-7613(1996)024%3c0949:ECOTNT%3e2.3.CO;2.
Teng LS, Lin AT. Cenozoic tectonics of the China continental margin: insights from Taiwan. Geol Soc Spec Pub. 2004;226(Aug):313–32. https://doi.org/10.1144/GSL.SP.2004.226.01.17.
Terzaghi RD. Sources of error in joint surveys. Geotechnique. 1965;15(3):287–304.
Tong LT, Ouyang S, Guo TR, Lee CLCRCL, Hu KH, Lee CLCRCL, Wang CJ. Insight into the geothermal structure in Chingshui, Ilan, Taiwan. Terr Atmos Ocean Sci. 2008;19(4):413–24. https://doi.org/10.3319/TAO.2008.19.4.413(T).
Townend J, Sutherland R, Toy VG, Eccles JD, Boulton C, Cox SC, McNamara D. Late-interseismic state of a continental plate-bounding fault: petrophysical results from DFDP-1 wireline logging and core analysis, Alpine Fault, New Zealand. Geochem Geophys Geosyst. 2013;14(9):3801–20. https://doi.org/10.1002/ggge.20236.
Tseng CS. Geology and geothermal occurrence of the Chingshui and Tuchang districts, Ilan. Pet Geol Taiwan. 1978;15:11–23.
Vidal J, Hehn R, Glaas C, Genter A. How can temperature logs help identify permeable fractures and define a conceptual model of fluid circulation? An example from deep geothermal wells in the Upper Rhine Graben. Geofluids. 2019. https://doi.org/10.1155/2019/3978364.
Wallis IC, McNamara DD, Rowland JV, Massiot C. The nature of fracture permeability in the basement greywacke at Kawerau geothermal Field, New Zealand. In: Proceedings of the Thirty-Seventh Workshop on Geothermal Reservoir Engineering, Stanford. 2012.
Yamada M, Iguchi K, Nakanishi S, Todaka N. Reservoir characteristics and development plan of the Oguni geothermal field, Kyushu, Japan. Geothermics. 2000;29(2):151–69. https://doi.org/10.1016/S0375-6505(99)00058-9.
Yeh EC, Sun TH, Lin ST, Lee WC, Lin W, Wu YM, Wang TT, Song SR, Lin W. Investigation of relationship between in-situ stress and fluid conduits from Chinshui geothermal area, NE Taiwan. In: AGU Fall Meeting. 2013. p. H51D–1218.
Yui TF, Liu KK, Shieh YN. Stable isotope systematics of argillite/slate from a deep well in the Chingshui geothermal field, Taiwan. Chem Geol. 1993;103(1–4):181–91. https://doi.org/10.1016/0009-2541(93)90300-8.
Zoback MD. Reservoir geomechanics. Cambridge: Cambridge University Press; 2007. https://doi.org/10.1017/CBO9780511586477.
Zoback MD, Barton CA, Brudy M, Castillo DA, Finkbeiner T, Grollimund BR, Moos DB, Peska P, Ward CD, Wiprut DJ. Determination of stress orientation and magnitude in deep wells. Int J Rock Mech Min Sci. 2003;40(7–8):1049–76. https://doi.org/10.1016/j.ijrmms.2003.07.001.

Publisher's Note